

# Progressive Content-aware Coded Hyperspectral Compressive Imaging

Xuanyu Zhang<sup>1</sup>, Bin Chen<sup>1</sup>, Wenzhen Zou<sup>2</sup>, Shuai Liu<sup>3</sup>, Yongbing Zhang<sup>2</sup>, Ruiqin Xiong<sup>4</sup>, Jian Zhang<sup>1</sup>  
<sup>1</sup>Peking University Shenzhen Graduate School <sup>2</sup>Harbin Institute of Technology (Shenzhen)  
<sup>3</sup>Tsinghua University <sup>4</sup>Peking University

## Abstract

Hyperspectral imaging plays a pivotal role in a wide range of applications, like remote sensing, medicine, and cytology. By acquiring 3D hyperspectral images (HSIs) via 2D sensors, the coded aperture snapshot spectral imaging (CASSI) has achieved great success due to its hardware-friendly implementation and fast imaging speed. However, for some less spectrally sparse scenes, single snapshot and unreasonable coded aperture design tend to make HSI recovery more ill-posed and yield poor spatial and spectral fidelity. In this paper, we propose a novel **Progressive Content-Aware CASSI** framework, dubbed **PCA-CASSI**, which captures HSIs with multiple optimized content-aware coded apertures and fuses all the snapshots for reconstruction progressively. Simultaneously, by mapping the Range-Null space Decomposition (RND) into a deep network with several phases, an RND-HRNet is proposed for HSI recovery. Each recovery phase can fully exploit the hidden physical information in the coded apertures via explicit  $\mathcal{R}$ - $\mathcal{N}$  decomposition and explore the spatial-spectral correlation by dual transformer blocks. Our method is validated to surpass other state-of-the-art methods on both multiple- and single-shot HSI imaging tasks by large margins.

## 1. Introduction

Hyperspectral images (HSIs) embody rich spectral bands and detailed information than the normal RGB images, which have unprecedented demand in recent years [57, 2, 9, 19]. Inspired by the compressive sensing (CS) [67, 62, 25, 10, 59, 47, 46, 21], CASSI system aims to utilize 2D detector to capture 3D hyperspectral scenes. Due to the merits of fast acquisition speed, low cost, and high data throughput, it has played an indispensable role in a wealth of applications, such as remote sensing, object detection, super-resolution, and medical diagnosis [68, 38, 33, 24, 52, 15, 49, 1]. However, for some specific applications, the information retained in a single snapshot is inadequate. For instance, mi-

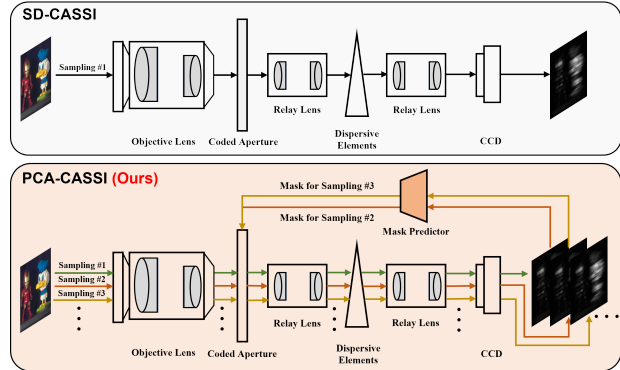


Figure 1. Illustration of SD-CASSI and the proposed PCA-CASSI system. SD-CASSI compresses the HSI via a single coded aperture and tends to cause excessive information loss. However, our PCA-CASSI captures the same HSI with multiple content-aware coded apertures (produced by the mask predictor) progressively, which significantly increases the information throughput.

croscopic imaging [4] has extremely high demands on the textures and details of the HSIs. To guarantee the accuracy of recovered images, capturing the same scene with multiple shots is necessary and imperative. Simultaneously, with the development of sampling devices, the improved digital micromirror device (DMD) [51] and CCD sensors allow the imaging system to record multiple snapshots and alter the coded patterns with a limited increase in acquisition time.

Although previous works such as MS-CASSI [23] have explored the potential of multiple shots, there are still several bottlenecks to be solved. **First**, how to design optimal multiple-coded apertures is the key to the enhancement of multiple snapshot imaging systems. We focus on the following two aspects: **1)** The coded apertures are expected to exhibit excellent anisotropy and complementarity. The complementary coded apertures promote the fusion and interaction of the multiple snapshots, otherwise they may tend to interfere with each other and undermine the beneficial information; **2)** Furthermore, the coded apertures are supposed to be adjusted contextually. Prior information from the previous shots enables coded apertures to perceive the content of HSIs, thus increasing the flexibility and performance of imaging systems. To the best of our knowledge,

Corresponding author: Jian Zhang (zhangjian.sz@pku.edu.cn).

these two aspects remain under-investigated. **Second**, existing reconstruction networks generally focus on the single disperser CASSI system (SD-CASSI). The practical solution for multiple-shot reconstruction is deficient. Meanwhile, how to utilize the coded aperture to retain the range space and recover the null space of HSIs has been ignored.

To solve the above-mentioned issues, a novel **Progressive Content-Aware Coded Aperture Snapshot Spectral Imaging** framework, dubbed **PCA-CASSI**, is proposed for progressive content-aware sampling and accurate multiple-shot reconstruction (Fig. 1). From hardware perspective, PCA-CASSI can be easily implemented from the original SD-CASSI [40] hardware with little modification. From algorithm perspective, PCA-CASSI is composed of the light-weight recovery network and mask predictor. Furthermore, an **Range-Null space Decomposition unfolding Hyperspectral Reconstruction Network (RND-HRNet)** is proposed to fuse all the coded measurements adaptively. Overall, our contributions are summarized as:

- A novel “**Encoder + Decoder**” framework, dubbed PCA-CASSI, is proposed to capture HSIs contextually and reconstruct them progressively. Noted that the “**Encoder**” corresponds to the HSI sampling while the “**Decoder**” actually indicates the HSI reconstruction.
- A progressive content-aware sampling strategy is proposed to perceive HSI contents and optimize the coded aperture in the current shot from the measurement in the previous shot.
- An  $\mathcal{R}-\mathcal{N}$  decomposition-inspired network, dubbed RND-HRNet, is presented to reconstruct HSIs, which utilizes the range-null space decomposition module (RNDM) to refine the null space of the HSIs iteratively and adopts the spectral spatial fusion module (SSFm) to exploit the non-local spatial-spectral information.
- Experiments exhibit that our method outperforms other state-of-the-art methods on both multiple- and single-shot HSI reconstruction tasks by large margins.

## 2. Related Works

### 2.1. Hyperspectral Imaging Systems

Conventional hyperspectral cameras usually make a trade-off between temporal and spectral resolution. Inspired by the theory of compressive sensing (CS), CASSI aims to capture hyperspectral images (HSIs) within a snapshot time. In what follows, we will review some representative works on imaging optical path and coded aperture design.

**Imaging Optical Path:** The most representative CASSI system [40] utilized a single disperser to encode spatial and spectral information. To improve the imaging performance and information throughput, Kittle *et al.* [23] captured the

same hyperspectral scenes via varied coded apertures. In addition, by temporally aligning the single-shot CASSI system with an RGB camera, Wang *et al.* [44] provided multi-modal supervision and complementary information for HSI reconstruction. Recently, Lin *et al.* [28, 27] utilized two high speed spatial light modulators to realize dual-optical coding. Although the optical path design of CASSI has achieved remarkable results, ensuring high compression ratio and excellent image quality is still a bottleneck.

**Coded Aperture Design:** Wu *et al.* [51] first introduced the digital micromirror device (DMD) into the imaging systems to realize flexible and fast dynamic coding. Benefiting from the rapid response time of DMD, the theory of Restricted Isometry Property (RIP) [17] was introduced to guide the coded aperture optimization. To make the coded aperture retain enough useful information and remove redundancy, Zhang *et al.* [66] combined the coded aperture optimization and HSI reconstruction with an united network to achieve efficient mask optimization. However, as the complex scene varies, designing adaptive, content-aware and task-driven coded apertures is worthy of exploration.

### 2.2. HSI Reconstruction Methods

**Model-based Methods:** The traditional model-based methods employ the regularization term inspired by the image prior to solve the ill-posed inverse problem iteratively with widely-used optimization frameworks, such as ISTA [3], GAP [56] and so on [31, 39]. Simultaneously, to improve the representation ability of the model, TV [56], GMM [54, 53], image sparsity representation [45] and rank minimization [29] are embedded into the above optimization frameworks to provide prior information. Although these methods produce decent results in specific scenarios, it is difficult to design suitable hand-crafted priors for all scenes.

**Deep Learning-based Methods:** Owing to the powerful representation capabilities of deep networks, learning-based HSI reconstruction methods [36] have received increasing attention. To improve the accuracy and perceptual quality, residual blocks [41], spatial-spectral attention modules [34], long-short-term memory units [13] and Fourier domain constraint [20] are embedded into the structure of convolution neural networks (CNNs). Although they can capture the local image cues, CNNs fail to exploit the global correlation and long-range dependencies. Recently, thanks to the wide application of vision transformers, spatial-wise and channel-wise transformers have been incorporated into the multi-scale encoder-decoder architectures [6, 5]. To alleviate the poor interpretability of these end-to-end networks, some researchers have attempted to combine optimization algorithms and deep network priors, such as plug-and-play frameworks [58, 69, 35]. Meanwhile, deep unfolding methods [42, 43, 64, 8, 22, 66] have been prevalent for its exquisite design and powerful performance. Although

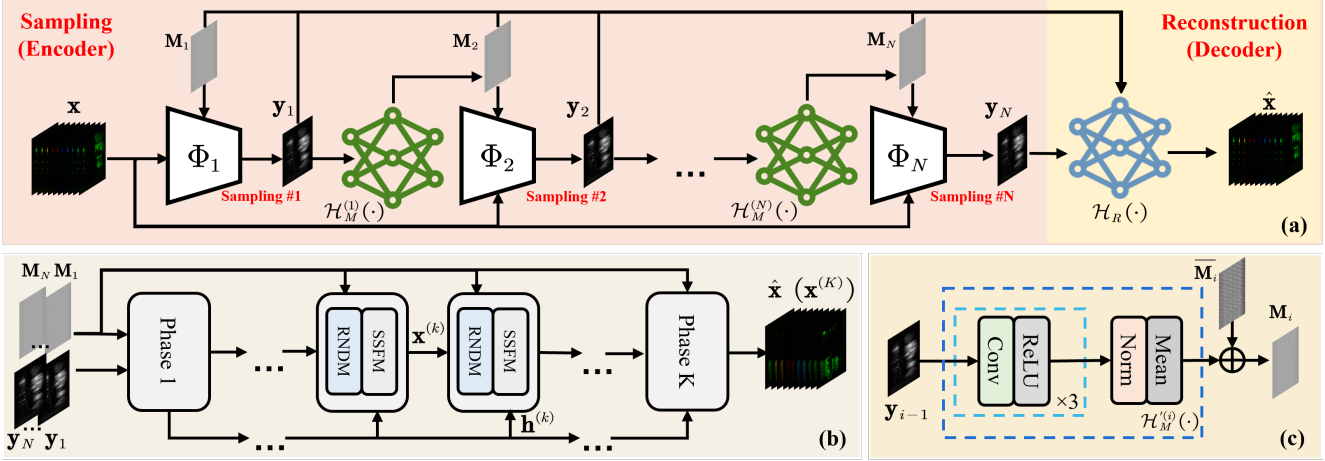


Figure 2. Illustration of the proposed PCA-CASSI. (a) overall architecture, (b)  $\mathcal{H}_R(\cdot)$ , (c)  $\mathcal{H}_M^{(i)}(\cdot)$ .  $\mathcal{H}_R(\cdot)$  takes multiple snapshots  $\{y_i\}_{i=1}^N$  and coded apertures  $\{M_i\}_{i=1}^N$  to generate the reconstructed HSI  $\hat{\mathbf{x}}$ , which includes  $K$  RND-inspired recovery phases. It is also adapted to single-shot reconstruction.  $\mathcal{H}_M^{(i)}(\cdot)$  takes the snapshot  $y_{i-1}$  from previous shot to predict the coded aperture  $M_i$  in the current shot.

these methods have achieved great success, few attention has been paid to the multiple-shot HSI reconstruction.

### 3. Proposed Method

#### 3.1. Review of the CASSI system

In CASSI, the 3D hyperspectral cube is first modulated via a coded aperture and then dispersed via a dispersive element (Fig. 1). Given a HSI sequence  $\{\mathbf{X}_i\}_{i=1}^C \in \mathbb{R}^{H \times W}$ , each frame is modulated via a coded aperture  $M \in \mathbb{R}^{H \times W}$ :

$$\mathbf{X}'_i = M \odot \mathbf{X}_i, \quad (1)$$

where  $\mathbf{X}'_i$  is the  $i^{\text{th}}$  modulated HSI frame and  $\odot$  denotes the Hadamard product. The modulated HSI frames  $\{\mathbf{X}'_i\}_{i=1}^C \in \mathbb{R}^{H \times W}$  with different wavelengths are then shifted spatially and summed in an element-wise manner, leading to a coded measurement:

$$\mathbf{Y}(m, n) = \sum_{i=1}^C \mathbf{X}'_i(m, n + d_i) + \mathbf{N}, \quad (2)$$

where  $(m, n)$  is the spatial coordinates, and  $d_i$  denotes the shifting distance of the  $i^{\text{th}}$  channel.  $\mathbf{N} \in \mathbb{R}^{H \times (W+C-1)}$  and  $\mathbf{Y} \in \mathbb{R}^{H \times (W+C-1)}$  denote the noise and the coded measurement, respectively. The vectorized form of CASSI is:

$$\mathbf{y} = \Phi \mathbf{x} + \mathbf{n}, \quad (3)$$

where  $\mathbf{x}$ ,  $\mathbf{y}$  and  $\mathbf{n}$  denote the vectorized form of  $\mathbf{X}$ ,  $\mathbf{Y}$  and  $\mathbf{N}$ , respectively.  $\Phi$  represents the sensing matrix.

The above imaging system can be extended to multiple shots. For instance, if we capture the same scene  $\mathbf{X}$  via  $N$  multiple different code apertures  $\{M_i\}_{i=1}^N$ , every shot can be treated as an implementation of the CASSI system. Hereby, the imaging scheme can be formulated as follows:

$$[\mathbf{y}_1^T, \mathbf{y}_2^T, \dots, \mathbf{y}_N^T]^T = [\Phi_1^T, \Phi_2^T, \dots, \Phi_N^T]^T \mathbf{x} + \mathbf{n}, \quad (4)$$

where  $\mathbf{y}_i$  and  $\Phi_i = \text{Mask2Mat}(M_i)$  denote the observed

HSI measurement and sensing matrix of the  $i^{\text{th}}$  shot, respectively.  $\text{Mask2Mat}(\cdot)$  transforms the physical mask  $M_i$  to its equivalent sensing matrix form  $\Phi_i$ . The degradation process of multiple-snapshot compressive imaging remains a linear model and can still be expressed as  $\mathbf{y} = \Phi \mathbf{x} + \mathbf{n}$ .

#### 3.2. Overview of the Proposed PCA-CASSI

As illustrated in Fig. 2, PCA-CASSI is a novel ‘‘Encoder + Decoder’’ framework, which aims to compress HSIs by various content-aware optimal masks to increase the information throughput and fuse all the captured snapshots for HSI restoration cooperatively. Note that following [5, 6], this work just focuses on hyperspectral image sampling and restoration, and our contributions may be extensible to other imaging systems like [40, 23, 65]. For software algorithm, it is composed of two sub-modules, namely the mask predictors  $\{\mathcal{H}_M^{(i)}(\cdot)\}_{i=1}^N$  and reconstruction network  $\mathcal{H}_R(\cdot)$ . The mask predictors  $\{\mathcal{H}_M^{(i)}(\cdot)\}_{i=1}^N$  are capable of generating the optimal mask contextually in the current shot from the measurement in the previous shot, which is formulated as:

$$M_i = \mathcal{H}_M^{(i)}(\mathbf{y}_{i-1}), \quad i \in \{2, 3, \dots\}, \quad (5)$$

where  $M_i$  denotes the mask in the  $i^{\text{th}}$  shot and  $\mathbf{y}_{i-1}$  represents the measurement in the  $(i-1)^{\text{th}}$  shot.  $M_1$  is a learnable parameter. We will elaborate this module in Sec. 3.3. Simultaneously,  $\mathcal{H}_R(\cdot)$  is designed to integrate all the coded snapshots based on the  $\mathcal{R}$ - $\mathcal{N}$  Decomposition (RND) theory, which is formulated as follows:

$$\hat{\mathbf{x}} = \mathcal{H}_R(\mathbf{y}_1, M_1, \mathbf{y}_2, M_2, \dots, \mathbf{y}_N, M_N), \quad (6)$$

where  $\hat{\mathbf{x}}$  denotes the reconstruction result. We will elaborate it in Sec 3.4. For hardware realization, the proposed PCA-CASSI can be easily implemented via the acquisition devices of SD-CASSI [40]. Owing to the rapid response

Table 1. High-level functional comparison among three representative imaging systems and our proposed PCA-CASSI.

Method	SD-CASSI [40]	DCD [65]	MS-CASSI [23]	PCA-CASSI
Single CCD sensor	✓	✗	✓	✓
Multiple mask switch	✗	✗	✓	✓
Progressive sampling	✗	✗	✗	✓
Content-aware mask	✗	✗	✗	✓

time of 2D sensors and the fast prediction speed of  $\mathcal{H}_M^{(i)}(\cdot)$ , the increased time caused by multiple shots is indeed limited. Considering its superior performance, it is still worth sacrificing a little sampling speed for higher imaging performance in some applications. As illustrated in Tab. 1, our framework is distinguished from some previous works. Different from MS-CASSI [23] which utilizes parallel multiple coded apertures in the optical path, the proposed PCA-CASSI can achieve progressive sampling sequentially and be easily extended to any number of shots. Different from DCD [18, 65], which uses dual cameras to capture snapshots and grayscale images simultaneously, our framework requires only one camera and is more flexible with respect to the coded apertures. Hence, the proposed PCA-CASSI is hardware-friendly in system implementation, content-aware in coded aperture design, and effective in HSI recovery.

### 3.3. Progressive Content-aware Sampling

Apart from the fusion mechanism in the restoration process, coded aperture design plays a pivotal role in PCA-CASSI, which enables different measurements to contain complementary information and maintain excellent anisotropy. Considering that different HSIs have various spectral correlations and spatial sparsities, the coded measurement from the previous shot is utilized to optimize the coded aperture in the current shot. Thereby, the optimized coded apertures tend to perceive the photographed HSIs and make content-aware adjustments adaptively. As the shot epoch progresses, the optimized coded apertures tend to be more reasonable with more accurate reconstruction results.

Specifically, as shown in Fig. 2 (a), the hyperspectral scene  $\mathbf{x}$  is firstly captured by the mask  $\mathbf{M}_1$  to obtain the measurement  $\mathbf{y}_1$ . Then, the coarse compressed result  $\mathbf{y}_1$  is adopted to furnish prior information and predict subsequent mask  $\mathbf{M}_2$ . Due to the guidance of  $\mathbf{y}_1$ ,  $\mathbf{M}_2$  is able to perceive the content of the HSIs and refine the coded pattern. Generally, the coded aperture  $\mathbf{M}_i$  in the  $i^{th}$  shot is generated from the measurement  $\mathbf{y}_{i-1}$  via the mask predictor  $\mathcal{H}_M^{(i)}(\cdot)$ . To be noted, the optimized mask in each shot is required to reflect both the shared properties of the imaging system and the independent characteristics of each HSI. Hence, the optimized masks  $\{\mathbf{M}_i\}_{i=1}^N$  are decoupled into two components, namely shared component and content-aware component. The shared components  $\{\overline{\mathbf{M}}_i\}_{i=1}^N$  are learnable parameters and jointly optimized in the network. The content-aware component is derived from the previous measurement  $\mathbf{y}_{i-1}$  via a lightweight deep module  $\mathcal{H}_M^{(i)}(\cdot)$ , composed of three

Conv-ReLU layers, a normalization layer and a mean layer (Fig. 2 (c)). The normalization layer transforms all pixels to the interval  $[0, 1]$ . The mean layer calculates the channel-wise means of features to produce the masks. The above pipeline, corresponding to Eq. 5, is implemented as:

$$\mathbf{M}_i = \mathcal{H}_M^{(i)}(\mathbf{y}_{i-1}) = \overline{\mathbf{M}}_i + \eta^{(i)} \cdot \mathcal{H}_M^{(i)}(\mathbf{y}_{i-1}), \quad (7)$$

where  $\eta^{(i)}$  denotes a learnable parameter to stabilize the network training. By means of our progressive content-aware sampling, each snapshot tends to capture complementary physical information and spectral features.

### 3.4. Architecture of the Proposed RND-HRNet

The proposed RND-HRNet aims to recover the hyper-spectral scene  $\mathbf{x}$  from the snapshots  $\{\mathbf{y}_i\}_{i=1}^N$  and use coded apertures  $\{\mathbf{M}_i\}_{i=1}^N$  to guide the transmission of spectral-spatial features. To start with the noise-free degradation model  $\mathbf{y} = \Phi \mathbf{x}$ , the HSI reconstruction is formulated as:

$$\hat{\mathbf{x}} = \arg \min_{\mathbf{x}} \frac{1}{2} \|\mathbf{y} - \Phi \mathbf{x}\|_2^2 + \lambda \psi(\mathbf{x}), \quad (8)$$

where  $\mathbf{y} = [\mathbf{y}_1^\top, \mathbf{y}_2^\top, \dots, \mathbf{y}_N^\top]^\top$  denotes the concatenation of all vectors of measurements. The first part is the data fidelity term, and the second part  $\lambda \psi(\mathbf{x})$  denotes the regularization term. Following the traditional ISTA framework [60, 61], Eq. 8 can be solved by iterating between the following gradient descent and proximal mapping steps:

$$\mathbf{r}^{(k)} = \mathbf{x}^{(k-1)} - \rho \Phi^\top (\Phi \mathbf{x}^{(k-1)} - \mathbf{y}), \quad (9)$$

$$\mathbf{x}^{(k)} = \text{prox}_{\lambda \psi}(\mathbf{r}^{(k)}), \quad (10)$$

where  $\mathbf{r}^{(k)}$  and  $\mathbf{x}^{(k)}$  denote the intermediate result and reconstruction image in the  $k^{th}$  phase, respectively.  $k$  and  $\rho$  denote the number of ISTA iterations and the step size, respectively. The limitation of the above Eq. 9 is that gradient descent can only find an approximate sub-optimal solution to the data fidelity term in each iteration, which cannot strictly satisfy  $\mathbf{y} \equiv \Phi \mathbf{r}^{(k)}$ . To tackle with the bottleneck of gradient descent, inspired by [11, 12], the  $\mathcal{R}-\mathcal{N}$  Decomposition (RND) is introduced to explicitly maintain the consistency constraint of the data fidelity term. Given a sensing matrix  $\Phi$  and its pseudo inverse matrix  $\Phi^\dagger$ , which satisfies  $\Phi \Phi^\dagger = \mathbf{I}$ , we have the following theorem for arbitrary HSIs:

**Theorem 1** ([11])  *$\mathcal{R}-\mathcal{N}$  Decomposition:* Let  $\mathcal{P}_r \triangleq \Phi^\dagger \Phi$  be the operator that projects the sample  $\mathbf{x}$  from sample domain to the range of  $\Phi^\dagger$ , and denote by  $\mathcal{P}_n \triangleq (\mathbf{I} - \Phi^\dagger \Phi)$  the operator that projects  $\mathbf{x}$  to the null space of  $\Phi$ . Then  $\forall \mathbf{x} \in \mathbb{R}^{H \times W \times C}$ , there exists the unique decomposition:

$$\mathbf{x} \equiv \mathcal{P}_r(\mathbf{x}) + \mathcal{P}_n(\mathbf{x}), \quad (11)$$

where  $\mathcal{P}_r(\mathbf{x})$  and  $\mathcal{P}_n(\mathbf{x})$  respectively denote the range and null space of  $\mathbf{x}$ . The HSI reconstruction can be treated as solving these two components  $\mathcal{P}_r(\mathbf{x})$  and  $\mathcal{P}_n(\mathbf{x})$ . Reconstructing the range space of the HSI signal is to ensure the

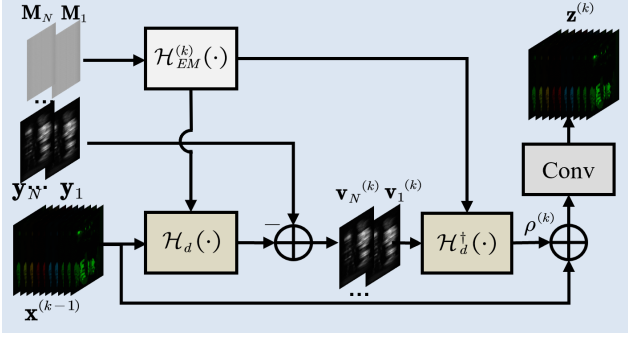


Figure 3. Details of the proposed RNDM. It retains the range-space component and recovers the null-space component of HSIs.

data consistency with respect to measurement  $\mathbf{y}$ , while refining the null space of the HSI signal aims to remove artifacts and enrich details. Therefore, the core advantage of RND lies in its ability to improve perceptual quality while maintaining reconstruction fidelity. Furthermore, substituting  $\mathbf{y} = \Phi \mathbf{x}$  into Eq. 11, we have the following RND for  $\mathbf{x}$ :

$$\mathbf{x} \equiv \Phi^\dagger \mathbf{y} + (\mathbf{I} - \Phi^\dagger \Phi) \mathbf{x}. \quad (12)$$

In HSI reconstruction, the range-space component  $\Phi^\dagger \mathbf{y}$  can actually be calculated from  $\mathbf{y}$ , while the null-space component  $[(\mathbf{I} - \Phi^\dagger \Phi) \mathbf{x}]$  can be refined and estimated by the network. To be noted, the combination of  $\Phi^\dagger \mathbf{y}$  and any solution  $\mathbf{s}$  for the null-space component projected by  $(\mathbf{I} - \Phi^\dagger \Phi)$  strictly enjoys the exact data consistency, *i.e.*  $\forall \mathbf{s}, \Phi [\Phi^\dagger \mathbf{y} + (\mathbf{I} - \Phi^\dagger \Phi) \mathbf{s}] \equiv \mathbf{y}$ . Thus, our motivation is to estimate the null-space component  $[(\mathbf{I} - \Phi^\dagger \Phi) \mathbf{x}]$  only and remain the clean range-space component unchanged to alleviate the recovery difficulty of networks. Furthermore, we unfold the null-space learning in Eq. 12 into a deep network and resort to the proximal mapping to refine the null-space correlated component iteratively as follows.

$$\begin{aligned} \mathbf{z}^{(k)} &= \Phi^\dagger \mathbf{y} + (\mathbf{I} - \Phi^\dagger \Phi) \mathbf{x}^{(k-1)} \\ &= \mathbf{x}^{(k-1)} + \Phi^\dagger (\mathbf{y} - \Phi \mathbf{x}^{(k-1)}), \end{aligned} \quad (13)$$

$$\mathbf{x}^{(k)} = \text{prox}_{\lambda\psi}(\mathbf{z}^{(k)}), \quad (14)$$

where  $\mathbf{z}^{(k)}$  and  $\mathbf{x}^{(k)}$  respectively denote the result of RND and proximal mapping in the  $k^{\text{th}}$  iteration. Inspired by Eq. 13 and Eq. 14, the range-null decomposition module (RNDM) and spatial-spectral fusion module (SSFM) are proposed as follows for accurate HSI reconstruction.

### 3.4.1 Range-Null Space Decomposition Module

Inspired by Eq. 13, our RNDM aims to retain the range space and refine the null space of the HSIs iteratively (Fig. 3). Given the snapshots  $\{\mathbf{y}_i\}_{i=1}^N$  and masks  $\{\mathbf{M}_i\}_{i=1}^N$ , RNDM yields the intermediate result  $\mathbf{z}^{(k)}$  flexibly.

$$\mathbf{z}^{(k)} = \text{RNDM}^{(k)}(\mathbf{x}^{(k-1)}, \mathbf{y}_1, \dots, \mathbf{y}_N, \mathbf{M}_1, \dots, \mathbf{M}_N). \quad (15)$$

Due to the cumulative errors caused by equipment deviation, noise corruption and alignment of the continuous spectrum in real scenes, using physical masks  $\{\mathbf{M}_i\}_{i=1}^N$  directly may be imprecise. Therefore, a deep enhanced module  $\mathcal{H}_{EM}^{(k)}(\cdot)$  is introduced to produce two enhanced mask representations  $\mathbf{F}_i^{(k)} \in \mathbb{R}^{H \times W \times C}$  and  $\mathbf{E}_i^{(k)} \in \mathbb{R}^{H \times W \times C}$  from the physical mask  $\mathbf{M}_i \in \mathbb{R}^{H \times W}$ , which corrects the bias between the degradation process and the physical mask via an attention mechanism [6] as follows.

$$\mathbf{F}_i^{(k)}, \mathbf{E}_i^{(k)} = \mathcal{H}_{EM}^{(k)}(\mathbf{M}_i). \quad (16)$$

Furthermore, the crucial step of RNDM is to solve the degradation operator  $\mathcal{H}_d(\cdot, \cdot)$  and its pseudo-inverse operator  $\mathcal{H}_d^\dagger(\cdot, \cdot)$ . Specifically,  $\mathcal{H}_d(\cdot, \cdot)$  simulates the process of mask modulation, dispersion, and compression in Sec. 3.1 with the current state  $\mathbf{x}^{(k-1)}$  and enhanced mask representations  $\mathbf{F}_i^{(k)}$ .  $\mathcal{H}_d^\dagger(\cdot, \cdot)$  is designed to provide an initialization from 2D signals to 3D cubes with the enhanced representation  $\mathbf{E}_i^{(k)}$ . **More details about these two operators are presented in SM.** To dynamically balance the contribution of range- and null-space signals, the learnable parameter  $\rho^{(k)}$  is incorporated into the optimization process. Hence, we can do  $\mathcal{R}-\mathcal{N}$  decomposition on each  $\mathbf{y}_i$  to get the intermediate results  $\{\mathbf{z}_i^{(k)}\}_{i=1}^N$ . Then, a  $1 \times 1$  convolution is utilized to adaptively merge  $\{\mathbf{z}_i^{(k)}\}_{i=1}^N$  into  $\mathbf{z}^{(k)}$  as follows, which is fed to the subsequent proximal mapping module.

$$\begin{aligned} \mathbf{v}_i^{(k)} &= \mathbf{y}_i - \mathcal{H}_d(\mathbf{x}_i^{(k-1)}, \mathbf{F}_i^{(k)}), \\ \mathbf{z}_i^{(k)} &= \mathbf{x}_i^{(k-1)} + \rho^{(k)} \mathcal{H}_d^\dagger(\mathbf{v}_i^{(k)}, \mathbf{E}_i^{(k)}), \\ \mathbf{z}^{(k)} &= \text{Conv}^{(k)}([\mathbf{z}_1^{(k)}, \dots, \mathbf{z}_N^{(k)}]), \end{aligned} \quad (17)$$

where  $\mathbf{v}_i^{(k)}$  and  $[\cdot]$  respectively denote the auxiliary variable and the channel-wise concatenation operation. The measurements compressed by various coded patterns reflect different HSI contents and fuse complementary information.

### 3.4.2 Spectral-Spatial Fusion Module

To implement Eq. 14 with deep networks, SSFM is adopted to refine the fused intermediate result  $\mathbf{z}^{(k)}$  and yield the reconstruction result  $\mathbf{x}^{(k)}$  (Fig. 5). Given that HSI representations are spatially sparse and spectrally correlated, capturing spatial interactions and spectral correlation are just as important. Inspired by the previous works [6, 63], the channel-wise and spatial-wise transformer blocks are plugged into the U-shaped architecture. The spatial-wise transformer block (STB) fuses the swin transformer block and residual convolution blocks to integrate local and non-local information. The channel-wise transformer block (CTB) encodes each feature frame into a token and explores



Table 3. Comparison results of the proposed method and state-of-the-art HSI reconstruction methods on the two-shot reconstruction. The best and second-best scores are **highlighted** and underlined. Here,  $\mathcal{H}_R(\cdot)$  in PCA-CASSI and RND-HRNet both include 2 phases.

Testing set	GAP-TV [56] ICIP 2016	ADMM-TV [56] ICIP 2016	TSA-Net [34] ECCV 2020	SRN [41] Arxiv 2021	HDNet [20] CVPR 2022	MST [6] CVPR 2022	MST++ [7] CVPRW 2022	CST [5] ECCV 2022	RND-HRNet Ours	PCA-CASSI Ours
Scene01	27.62 / 0.739	27.85 / 0.768	33.62/0.912	34.79 / 0.930	35.20 / 0.941	35.50 / 0.942	35.89 / 0.947	35.57 / 0.939	<u>37.49 / 0.961</u>	<b>39.49 / 0.970</b>
Scene02	25.92 / 0.665	25.65 / 0.684	32.51/0.893	35.09 / 0.920	36.00 / 0.945	36.00 / 0.939	36.70 / 0.946	35.99 / 0.940	<u>39.78 / 0.969</u>	<b>43.52 / 0.984</b>
Scene03	23.65 / 0.762	23.84 / 0.791	33.89/0.932	34.50 / 0.930	35.01 / 0.936	36.38 / 0.943	36.44 / 0.947	35.94 / 0.943	<u>39.01 / 0.957</u>	<b>40.91 / 0.968</b>
Scene04	34.20 / 0.872	33.56 / 0.886	40.40/0.964	40.94 / 0.955	41.19 / 0.968	43.16 / 0.975	43.56 / 0.975	42.32 / 0.965	<u>44.49 / 0.980</u>	<b>47.44 / 0.988</b>
Scene05	23.90 / 0.708	23.94 / 0.732	31.05/0.917	32.21 / 0.925	32.76 / 0.946	33.31 / 0.946	33.18 / 0.948	33.25 / 0.945	<u>35.62 / 0.965</u>	<b>38.45 / 0.978</b>
Scene06	23.97 / 0.670	23.85 / 0.698	33.04/0.930	35.63 / 0.938	36.10 / 0.958	35.91 / 0.954	36.52 / 0.960	36.36 / 0.955	<u>38.47 / 0.970</u>	<b>40.15 / 0.980</b>
Scene07	23.46 / 0.682	23.60 / 0.712	32.06/0.902	33.63 / 0.919	33.44 / 0.917	33.70 / 0.916	33.96 / 0.918	34.02 / 0.921	<u>36.27 / 0.945</u>	<b>38.72 / 0.963</b>
Scene08	23.68 / 0.654	23.93 / 0.695	31.37/0.919	34.45 / 0.933	34.96 / 0.958	35.07 / 0.951	35.58 / 0.961	35.62 / 0.954	<u>37.58 / 0.971</u>	<b>39.48 / 0.981</b>
Scene09	25.18 / 0.708	25.04 / 0.743	32.27/0.913	34.27 / 0.930	34.42 / 0.937	36.15 / 0.944	35.89 / 0.945	35.52 / 0.942	<u>38.69 / 0.963</u>	<b>40.35 / 0.973</b>
Scene10	24.22 / 0.589	24.54 / 0.603	30.42/0.887	33.82 / 0.942	33.95 / 0.958	34.50 / 0.954	34.67 / 0.958	34.83 / 0.956	<u>36.54 / 0.971</u>	<b>38.78 / 0.981</b>
Average	25.58 / 0.705	25.58 / 0.731	33.06/0.917	34.93 / 0.932	35.30 / 0.947	35.97 / 0.946	36.24 / 0.951	35.94 / 0.946	<u>38.39 / 0.965</u>	<b>40.73 / 0.977</b>

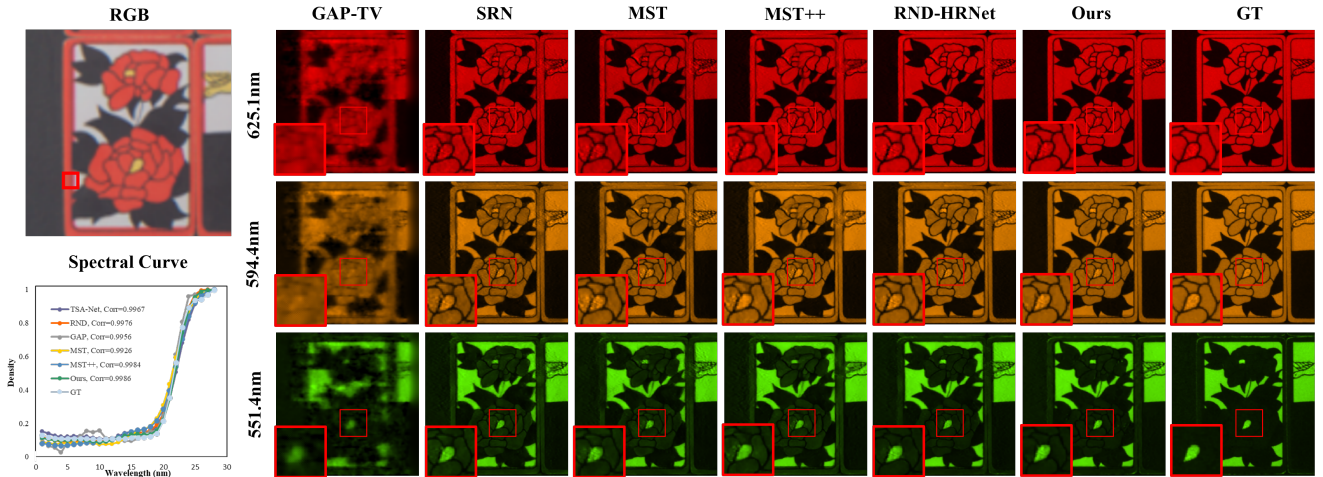


Figure 6. The visual comparison of the proposed method and other SOTA methods on the multiple-shot reconstruction.

dataset. Following [34], the simulation experiments are conducted on the public HSI datasets CAVE [55] and KAIST [14] with the size  $256 \times 256 \times 28$ . Meanwhile, 5 real compressive measurements [22] with the size of  $660 \times 714$  are used for testing. The metrics of PSNR and SSIM [48] are employed to evaluate the reconstruction quality.

## 4.2. Simulation Results

To demonstrate the effectiveness of the proposed PCA-CASSI and RND-HRNet, we compare our methods with other state-of-the-art (SOTA) methods, including model-based methods [56], classical CNN-based methods [41, 34, 22, 20] and recent transformer networks [6, 5, 7].

**Single-shot Reconstruction:** Following the settings of previous works [34, 22], we conduct the single-shot reconstruction on the KAIST dataset [14]. It can be clearly seen that the proposed RND-HRNet with 10 phases yields 38.54 dB on PSNR and 0.969 on SSIM, which significantly outperforms the most recent works [6, 5, 7] **over 2dB**. To be noted, even with only 2 phases, the proposed RND-HRNet can also achieve the current best performance. As exhibited in Fig. 4, our method can recover sharper edges and more realistic details, which indicates that the proposed RNDM and SSFM can accurately maintain data consistency and ef-

Table 4. Evaluation of computational complexity on multiple- and single-shot reconstructions. “Ph” denotes the number of Phases.

Method	Shot	Testing time	Params.	PSNR	SSIM
HDNet [20]	#1	116.92ms	2.37M	34.97dB	0.943
MST [6]	#1	176.36ms	2.03M	35.18dB	0.948
CST [5]	#1	153.18ms	1.36M	35.31dB	0.947
RND-HRNet-2Ph	#1	189.13ms	1.82M	36.66dB	0.957
RND-HRNet-10Ph	#1	531.37ms	9.48M	38.54dB	0.969
HDNet [20]	#2	117.45ms	2.37M	35.30dB	0.947
MST [6]	#2	179.25ms	2.03M	35.97dB	0.946
CST [5]	#2	159.21ms	1.36M	35.94dB	0.946
RND-HRNet-2Ph	#2	199.21ms	1.82M	38.39dB	0.965
PCA-CASSI-2Ph	#2	249.45ms	1.84M	40.73dB	0.977

fectively exploit the non-local correlation.

**Multiple-shot Reconstruction:** In this section, we extend the RND-HRNet to multiple-shot with the proposed progressive content-aware sampling. For PCA-CASSI, two optimized masks are utilized to capture HSIs respectively. For other methods, we adopt two fixed real masks, namely  $M$  [34] and  $1-M$ , to realize the two-shot imaging. To adapt existing methods to multiple-shot reconstruction, we utilize a few  $1 \times 1$  convolutions to fuse two measurements and masks in learning-based methods (SRN, HDNet, MST, CST). Besides, for model-based methods (GAP-TV, ADMM-TV), we jointly solve these two sub-optimization problems.

As shown in Tab. 3, all reconstruction methods have achieved corresponding improvements compared to single-

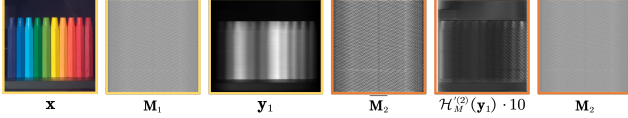


Figure 7. Visualization results of the optimized  $M_1$  and  $M_2$ , where  $M_2 = \overline{M}_2 + \eta^{(2)} \cdot \mathcal{H}_M^{(2)}(y_1)$ . For clearer presentation, all the element values of  $\mathcal{H}_M^{(2)}(y_1)$  are magnified by 10.

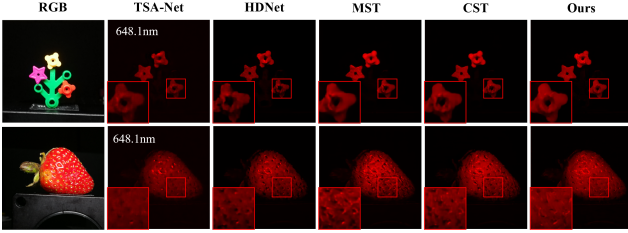


Figure 8. Real data results of the proposed RND-HRNet and other SOTA methods on the single-shot reconstruction.

shot results listed in Tab. 2. However, since the fusion method does not fully utilize the complementary information of multiple masks, some methods do not reach their limit of performance. Owing to the proposed RND-inspired fusion mechanism, RND-HRNet with 2 phases achieves 38.39dB on PSNR and 0.965 on SSIM, which surpasses 1.73 dB than the single-shot case. Noted that even utilizing the exact same system and masks, the proposed RND-HRNet also outperforms the SOTA method MST++ [7] by 2.15 dB on PSNR. Considering the trade-off between computational complexity and performance, RND-HRNet with 10 phases is not conducted on the multiple-shot case. Furthermore, utilizing the content-aware optimized masks, the proposed PCA-CASSI achieves very impressive results, *i.e.* 40.73dB on PSNR and 0.977 on SSIM. Compared with two recent SOTA methods CST [5] and MST [6], our method surpasses them by 4.79dB and 4.76dB on PSNR, which verifies the effect of the proposed imaging framework. As depicted in Fig. 6, the HSIs produced by our methods have clearer spatial details and more accurate spectral consistency. Meanwhile, Fig. 7 presents the content-aware optimized masks. An interesting finding is that the optimized mask  $M_2$  contains a shared pattern  $\overline{M}_2$  and veils some content-aware textures  $\mathcal{H}_M^{(2)}(y_1)$ .

**Computational complexity:** As listed in Tab. 4, the proposed RND-HRNet achieves greater performance than that of CST and MST with the same level of average testing time and even less parameters, which verifies the effect of the proposed RND-HRNet. With the mask predictor, the proposed method with 2 phases can obtain 2.34dB gains on PSNR with only 0.02M increase in parameters, proving the practicality of the progressive content-aware sampling.

### 4.3. Real Data Results

To objectively evaluate the proposed method on real data, RND-HRNet is tested in 5 real measurements [22].

Table 5. Evaluation of different mask combinations. Here, the reconstruction network includes 1 phase for simplicity. More results of the  $N$ -shot cases ( $N \geq 3$ ) are presented in our SM.

Case	Mask Type		Content-aware	PSNR	SSIM
	Fixed mask	Optimized mask			
1	1	0	✗	35.04	0.948
2	0	1	✗	36.33	0.957
3	1	1	✗	38.29	0.967
4	2	0	✗	35.73	0.953
5	0	2	✗	39.19	0.972
6	0	2	✓	39.62	0.974

To simulate the real imaging situations, 11-bit shot noise is injected into the training data [34]. As shown in Fig. 8, our results can reconstruct clearer HSI contents and detailed textures with fewer artifacts and noise, especially in the cropped regions such as flowers and strawberries, suggesting the generalization ability and robustness of our method.

### 4.4. Ablation Study

To evaluate the contribution of the proposed PCA-CASSI, we deploy the CASSI system on different mask combinations. For convenience, the reconstruction network is a one-phase RND-HRNet. Tab. 5 indicates the PSNR and SSIM on different mask combinations.

**Multiple-shot vs. Single-shot:** Comparing case 1 and case 4 or case 2 and case 5, HSI reconstruction with two fixed or optimized masks surpasses one-shot reconstruction by 0.69dB or 2.86dB on PSNR, suggesting that multiple complementary coded apertures capture richer information.

**Optimized vs. Fixed:** As shown in Tab. 5, the more optimized masks are used, the better the reconstruction performance is, indicating that more optimized masks better remove redundancy and retain useful information (case 2,3,5).

**Content-aware vs. Shared:** Comparing case 5 and case 6, we find that although randomly optimized masks are conducive to information acquisition, the same coded apertures are shared and non-adaptive for all HSI scenes, which inevitably leads to the loss of spectral anisotropy. With the proposed progressive content-aware strategy, HSI reconstruction with content-aware optimized masks can surpass the results with shared optimized masks by 0.43dB, which proves the effect of our mask optimization algorithm.

## 5. Conclusion

In this paper, we propose a novel spectral snapshot compressive imaging framework, dubbed PCA-CASSI. It progressively compresses HSIs with content-aware optimized coded apertures and fuses all the snapshots for reconstruction. Inspired by the  $\mathcal{R}-\mathcal{N}$  decomposition, an RND-HRNet is proposed for accurate HSI reconstruction. To improve its representation ability, a range-null space decomposition module is proposed to refine the null-space component of HSIs iteratively. Meanwhile, a spatial-spectral fusion module is introduced to explore the non-local correlation via

dual transformer blocks. Extensive experiments verify that our method significantly outperforms the other SOTA methods on both multiple- and single-shot reconstruction tasks.

## References

- [1] Hamed Akbari, Yukio Kosugi, Kazuyuki Kojima, and Naofumi Tanaka. Detection and analysis of the intestinal ischemia using visible and invisible hyperspectral imaging. *IEEE Transactions on Biomedical Engineering*, 57(8):2011–2017, 2010. **1**
- [2] Gonzalo R Arce, David J Brady, Lawrence Carin, Henry Arguello, and David S Kittle. Compressive coded aperture spectral imaging: an introduction. *IEEE Signal Processing Magazine*, 31(1):105–115, 2013. **1**
- [3] José M Bioucas-Dias and Mário AT Figueiredo. A new twist: two-step iterative shrinkage/thresholding algorithms for image restoration. *IEEE Transactions on Image Processing*, 16(12):2992–3004, 2007. **2**
- [4] Andrew Bullen. Microscopic imaging techniques for drug discovery. *Nature Reviews Drug Discovery*, 7(1):54–67, 2008. **1**
- [5] Yuanhao Cai, Jing Lin, Xiaowan Hu, Haoqian Wang, Xin Yuan, Yulun Zhang, Radu Timofte, and Luc Van Gool. Coarse-to-fine sparse transformer for hyperspectral image reconstruction. In *Proceedings of the European Conference on Computer Vision*, 2022. **2, 3, 6, 7, 8, 14**
- [6] Yuanhao Cai, Jing Lin, Xiaowan Hu, Haoqian Wang, Xin Yuan, Yulun Zhang, Radu Timofte, and Luc Van Gool. Mask-guided spectral-wise transformer for efficient hyperspectral image reconstruction. In *Proceedings of the IEEE/CVF Conference on Computer Vision and Pattern Recognition*, 2022. **2, 3, 5, 6, 7, 8, 13, 14**
- [7] Yuanhao Cai, Jing Lin, Zudi Lin, Haoqian Wang, Yulun Zhang, Hanspeter Pfister, Radu Timofte, and Luc Van Gool. Mst++: Multi-stage spectral-wise transformer for efficient spectral reconstruction. In *Proceedings of the IEEE/CVF Conference on Computer Vision and Pattern Recognition*, 2022. **6, 7, 8**
- [8] Yuanhao Cai, Jing Lin, Haoqian Wang, Xin Yuan, Henghui Ding, Yulun Zhang, Radu Timofte, and Luc Van Gool. Degradation-aware unfolding half-shuffle transformer for spectral compressive imaging. In *Proceedings of the Advances in Neural Information Processing Systems*, 2022. **2**
- [9] Xun Cao, Tao Yue, Xing Lin, Stephen Lin, Xin Yuan, Qionghai Dai, Lawrence Carin, and David J Brady. Computational snapshot multispectral cameras: toward dynamic capture of the spectral world. *IEEE Signal Processing Magazine*, 33(5):95–108, 2016. **1**
- [10] Bin Chen and Jian Zhang. Content-aware scalable deep compressed sensing. *IEEE Transactions on Image Processing*, 31:5412–5426, 2022. **1**
- [11] Dongdong Chen and Mike E Davies. Deep decomposition learning for inverse imaging problems. In *Proceedings of the European Conference on Computer Vision*, 2020. **4**
- [12] Dongdong Chen, Julián Tachella, and Mike E Davies. Equivariant imaging: Learning beyond the range space. In *Proceedings of the IEEE/CVF International Conference on Computer Vision*, pages 4379–4388, 2021. **4**
- [13] Ziheng Cheng, Bo Chen, Ruiying Lu, Zhengjue Wang, Hao Zhang, Ziyi Meng, and Xin Yuan. Recurrent neural networks for snapshot compressive imaging. *IEEE Transactions on Pattern Analysis and Machine Intelligence*, 45(2):2264–2281, 2023. **2**
- [14] Inchang Choi, MH Kim, D Gutierrez, DS Jeon, and G Nam. High-quality hyperspectral reconstruction using a spectral prior. *ACM Transactions on Graphics*, 36(6):1–13, 2017. **7**
- [15] Meng Ding, Xiao Fu, Ting-Zhu Huang, Jun Wang, and Xi-Le Zhao. Hyperspectral super-resolution via interpretable block-term tensor modeling. *IEEE Journal of Selected Topics in Signal Processing*, 15(3):641–656, 2020. **1**
- [16] Kingma DP and Jimmy Ba. Adam: a method for stochastic optimization. In *Proceedings of the International Conference for Learning Representations*, 2015. **6**
- [17] Yonina C Eldar and Gitta Kutyniok. *Compressed sensing: theory and applications*. Cambridge University Press, 2012. **2**
- [18] Ying Fu, Tao Zhang, Lizhi Wang, and Hua Huang. Coded hyperspectral image reconstruction using deep external and internal learning. *IEEE Transactions on Pattern Analysis and Machine Intelligence*, 44(7):3404–3420, 2021. **4**
- [19] Wei He, Naoto Yokoya, and Xin Yuan. Fast hyperspectral image recovery of dual-camera compressive hyperspectral imaging via non-iterative subspace-based fusion. *IEEE Transactions on Image Processing*, 30:7170–7183, 2021. **1**
- [20] Xiaowan Hu, Yuanhao Cai, Jing Lin, Haoqian Wang, Xin Yuan, Yulun Zhang, Radu Timofte, and Luc Van Gool. Hd-net: High-resolution dual-domain learning for spectral compressive imaging. In *Proceedings of the IEEE Conference on Computer Vision and Pattern Recognition*, 2022. **2, 6, 7, 14**
- [21] Yujie Hu, Yinhuai Wang, and Jian Zhang. Dear-gan: Degradation-aware face restoration with gan prior. *IEEE Transactions on Circuits and Systems for Video Technology*, 2023. **1**
- [22] Tao Huang, Weisheng Dong, Xin Yuan, Jinjian Wu, and Guangming Shi. Deep gaussian scale mixture prior for spectral compressive imaging. In *Proceedings of the IEEE/CVF Conference on Computer Vision and Pattern Recognition*, 2021. **2, 6, 7, 8, 12, 14**
- [23] David Kittle, Kerkil Choi, Ashwin Wagadarikar, and David J Brady. Multiframe image estimation for coded aperture snapshot spectral imagers. *Applied Optics*, 49(36):6824–6833, 2010. **1, 2, 3, 4**
- [24] Jie Lei, Weiyang Xie, Jian Yang, Yunsong Li, and Chein-I Chang. Spectral-spatial feature extraction for hyperspectral anomaly detection. *IEEE Transactions on Geoscience and Remote Sensing*, 57(10):8131–8143, 2019. **1**
- [25] Weiqi Li, Bin Chen, and Jian Zhang. D3c2-net: Dual-domain deep convolutional coding network for compressive sensing. *arXiv preprint arXiv:2207.13560*, 2022. **1**
- [26] Jingyun Liang, Jiezhong Cao, Guolei Sun, Kai Zhang, Luc Van Gool, and Radu Timofte. Swinir: Image restoration using swin transformer. In *Proceedings of the IEEE International Conference on Computer Vision*, 2021. **13**

- [27] Xing Lin, Yebin Liu, Jiamin Wu, and Qionghai Dai. Spatial-spectral encoded compressive hyperspectral imaging. *ACM Transactions on Graphics (TOG)*, 33(6):1–11, 2014. 2
- [28] Xing Lin, Gordon Wetzstein, Yebin Liu, and Qionghai Dai. Dual-coded compressive hyperspectral imaging. *Optics Letters*, 39(7):2044–2047, 2014. 2
- [29] Yang Liu, Xin Yuan, Jinli Suo, David J Brady, and Qionghai Dai. Rank minimization for snapshot compressive imaging. *IEEE Transactions on Pattern Analysis and Machine Intelligence*, 41(12):2990–3006, 2018. 2
- [30] Ze Liu, Yutong Lin, Yue Cao, Han Hu, Yixuan Wei, Zheng Zhang, Stephen Lin, and Baining Guo. Swin transformer: Hierarchical vision transformer using shifted windows. In *Proceedings of the IEEE International Conference on Computer Vision*, 2021. 13
- [31] Jiawei Ma, Xiao-Yang Liu, Zheng Shou, and Xin Yuan. Deep tensor admm-net for snapshot compressive imaging. In *Proceedings of the IEEE/CVF International Conference on Computer Vision*, 2019. 2
- [32] Qing Ma, Junjun Jiang, Xianming Liu, and Jiayi Ma. Deep unfolding network for spatio-spectral image super-resolution. *IEEE Transactions on Computational Imaging*, 8:28–40, 2021. 16
- [33] Farid Melgani and Lorenzo Bruzzone. Classification of hyperspectral remote sensing images with support vector machines. *IEEE Transactions on Geoscience and Remote Sensing*, 42(8):1778–1790, 2004. 1
- [34] Ziyi Meng, Jiawei Ma, and Xin Yuan. End-to-end low cost compressive spectral imaging with spatial-spectral self-attention. In *Proceedings of European Conference on Computer Vision*, 2020. 2, 6, 7, 8, 14
- [35] Ziyi Meng, Zhenming Yu, Kun Xu, and Xin Yuan. Self-supervised neural networks for spectral snapshot compressive imaging. In *Proceedings of the IEEE International Conference on Computer Vision*, 2021. 2
- [36] Xin Miao, Xin Yuan, Yunchen Pu, and Vassilis Athitsos.  $\lambda$ -net: reconstruct hyperspectral images from a snapshot measurement. In *Proceedings of the IEEE International Conference on Computer Vision*, 2019. 2, 14
- [37] Chong Mou, Qian Wang, and Jian Zhang. Deep generalized unfolding networks for image restoration. In *Proceedings of the IEEE/CVF Conference on Computer Vision and Pattern Recognition*, pages 17399–17410, 2022. 16
- [38] Lujendra Ojha, Mary Beth Wilhelm, Scott L Murchie, Alfred S McEwen, James J Wray, Jennifer Hanley, Marion Massé, and Matt Chojnacki. Spectral evidence for hydrated salts in recurring slope lineae on mars. *Nature Geoscience*, 8(11):829–832, 2015. 1
- [39] Jin Tan, Yanting Ma, Hoover Rueda, Dror Baron, and Gonzalo R Arce. Compressive hyperspectral imaging via approximate message passing. *IEEE Journal of Selected Topics in Signal Processing*, 10(2):389–401, 2015. 2
- [40] Ashwin Wagadarikar, Renu John, Rebecca Willett, and David Brady. Single disperser design for coded aperture snapshot spectral imaging. *Applied Optics*, 47(10):B44–B51, 2008. 2, 3, 4, 16
- [41] Jiamian Wang, Yulun Zhang, Xin Yuan, Yun Fu, and Zhiqiang Tao. A new backbone for hyperspectral image reconstruction. *arXiv preprint arXiv:2108.07739*, 2021. 2, 6, 7
- [42] Lizhi Wang, Chen Sun, Ying Fu, Min H Kim, and Hua Huang. Hyperspectral image reconstruction using a deep spatial-spectral prior. In *Proceedings of the IEEE/CVF Conference on Computer Vision and Pattern Recognition*, 2019. 2
- [43] Lizhi Wang, Chen Sun, Maoqing Zhang, Ying Fu, and Hua Huang. Dnu: deep non-local unrolling for computational spectral imaging. In *Proceedings of the IEEE/CVF Conference on Computer Vision and Pattern Recognition*, 2020. 2
- [44] Lizhi Wang, Zhiwei Xiong, Dahua Gao, Guangming Shi, and Feng Wu. Dual-camera design for coded aperture snapshot spectral imaging. *Applied Optics*, 54(4):848–858, 2015. 2
- [45] Lizhi Wang, Zhiwei Xiong, Guangming Shi, Feng Wu, and Wenjun Zeng. Adaptive nonlocal sparse representation for dual-camera compressive hyperspectral imaging. *IEEE Transactions on Pattern Analysis and Machine Intelligence*, 39(10):2104–2111, 2016. 2
- [46] Yinhuai Wang, Yujie Hu, Jiwen Yu, and Jian Zhang. Gan prior based null-space learning for consistent super-resolution. *arXiv preprint arXiv:2211.13524*, 2022. 1
- [47] Yinhuai Wang, Jiwen Yu, and Jian Zhang. Zero-shot image restoration using denoising diffusion null-space model. In *Proceedings of the International Conference on Learning Representations*, 2022. 1
- [48] Zhou Wang, Alan C Bovik, Hamid R Sheikh, and Eero P Simoncelli. Image quality assessment: from error visibility to structural similarity. *IEEE Transactions on Image Processing*, 13(4):600–612, 2004. 7
- [49] Xueling Wei, Wei Li, Mengmeng Zhang, and Qingli Li. Medical hyperspectral image classification based on end-to-end fusion deep neural network. *IEEE Transactions on Instrumentation and Measurement*, 68(11):4481–4492, 2019. 1
- [50] Zhuoyuan Wt, Jian Zhang, and Chong Mou. Dense deep unfolding network with 3d-cnn prior for snapshot compressive imaging. In *2021 IEEE/CVF International Conference on Computer Vision (ICCV)*, 2021. 16
- [51] Yuehao Wu, Iftexhar O Mirza, Gonzalo R Arce, and Dennis W Prather. Development of a digital-micromirror-device-based multishot snapshot spectral imaging system. *Optics Letters*, 36(14):2692–2694, 2011. 1, 2
- [52] Weiyang Xie, Tao Jiang, Yunsong Li, Xiuping Jia, and Jie Lei. Structure tensor and guided filtering-based algorithm for hyperspectral anomaly detection. *IEEE Transactions on Geoscience and Remote Sensing*, 57(7):4218–4230, 2019. 1
- [53] Jianbo Yang, Xuejun Liao, Xin Yuan, Patrick Lull, David J Brady, Guillermo Sapiro, and Lawrence Carin. Compressive sensing by learning a gaussian mixture model from measurements. *IEEE Transactions on Image Processing*, 24(1):106–119, 2014. 2
- [54] Jianbo Yang, Xin Yuan, Xuejun Liao, Patrick Lull, David J Brady, Guillermo Sapiro, and Lawrence Carin. Video compressive sensing using gaussian mixture models.

- IEEE Transactions on Image Processing*, 23(11):4863–4878, 2014. [2](#)
- [55] Fumihito Yasuma, Tomoo Mitsunaga, Daisuke Iso, and Shree K Nayar. Generalized assorted pixel camera: post-capture control of resolution, dynamic range, and spectrum. *IEEE Transactions on Image Processing*, 19(9):2241–2253, 2010. [7](#)
- [56] Xin Yuan. Generalized alternating projection based total variation minimization for compressive sensing. In *Proceedings of IEEE International Conference on Image Processing*, 2016. [2](#), [6](#), [7](#)
- [57] Xin Yuan, David J Brady, and Aggelos K Katsaggelos. Snapshot compressive imaging: theory, algorithms, and applications. *IEEE Signal Processing Magazine*, 38(2):65–88, 2021. [1](#)
- [58] Xin Yuan, Yang Liu, Jinli Suo, and Qionghai Dai. Plug-and-play algorithms for large-scale snapshot compressive imaging. In *Proceedings of the IEEE/CVF Conference on Computer Vision and Pattern Recognition*, 2020. [2](#)
- [59] Jian Zhang, Bin Chen, Ruiqin Xiong, and Yongbing Zhang. Physics-inspired compressive sensing: Beyond deep unrolling. *IEEE Signal Processing Magazine*, 40(1):58–72, 2023. [1](#)
- [60] Jian Zhang and Bernard Ghanem. Ista-net: interpretable optimization-inspired deep network for image compressive sensing. In *Proceedings of the IEEE/CVF Conference on Computer Vision and Pattern Recognition*, 2018. [4](#)
- [61] Jian Zhang, Chen Zhao, and Wen Gao. Optimization-inspired compact deep compressive sensing. *IEEE Journal of Selected Topics in Signal Processing*, 14(4):765–774, 2020. [4](#)
- [62] Jian Zhang, Chen Zhao, Debin Zhao, and Wen Gao. Image compressive sensing recovery using adaptively learned sparsifying basis via  $l_0$  minimization. *Signal Processing*, 103:114–126, 2014. [1](#)
- [63] Kai Zhang, Yawei Li, Jingyun Liang, Jiezhang Cao, Yulun Zhang, Hao Tang, Radu Timofte, and Luc Van Gool. Practical blind denoising via swin-conv-unet and data synthesis. *arXiv preprint arXiv:2203.13278*, 2022. [5](#), [13](#)
- [64] Shipeng Zhang, Lizhi Wang, Lei Zhang, and Hua Huang. Learning tensor low-rank prior for hyperspectral image reconstruction. In *Proceedings of the IEEE/CVF Conference on Computer Vision and Pattern Recognition*, 2021. [2](#)
- [65] Tao Zhang, Ying Fu, Lizhi Wang, and Hua Huang. Hyperspectral image reconstruction using deep external and internal learning. In *Proceedings of the IEEE/CVF International Conference on Computer Vision*, 2019. [3](#), [4](#)
- [66] Xuanyu Zhang, Yongbing Zhang, Ruiqin Xiong, Qilin Sun, and Jian Zhang. Herosnet: Hyperspectral explicable reconstruction and optimal sampling deep network for snapshot compressive imaging. In *Proceedings of the IEEE/CVF Conference on Computer Vision and Pattern Recognition*, 2022. [2](#), [6](#)
- [67] Chen Zhao, Siwei Ma, Jian Zhang, Ruiqin Xiong, and Wen Gao. Video compressive sensing reconstruction via reweighted residual sparsity. *IEEE Transactions on Circuits and Systems for Video Technology*, 27(6):1182–1195, 2016. [1](#)
- [68] Ji Zhao, Yanfei Zhong, Yunyun Wu, Liangpei Zhang, and Hong Shu. Sub-pixel mapping based on conditional random fields for hyperspectral remote sensing imagery. *IEEE Journal of Selected Topics in Signal Processing*, 9(6):1049–1060, 2015. [1](#)
- [69] Siming Zheng, Yang Liu, Ziyi Meng, Mu Qiao, Zhishen Tong, Xiaoyu Yang, Shensheng Han, and Xin Yuan. Deep plug-and-play priors for spectral snapshot compressive imaging. *Photonics Research*, 9(2):B18–B29, 2021. [2](#)

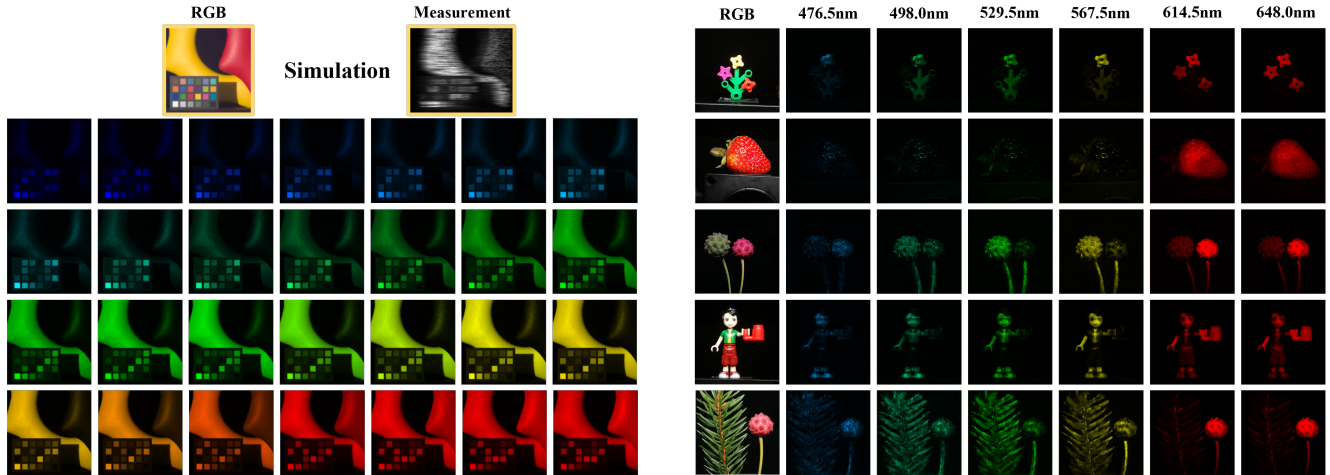


Figure 9. Reconstructed results of the proposed methods. Simulation results of all 28 bands [22] are presented in the left column and the real data results are shown in the right column.

In the supplementary materials, we demonstrate additional experimental results and implementation details as follows.

- Implementation details of some key modules are elaborated in Sec. A;
- More visualizations of the real reconstruction results, simulation results, and content-aware masks are shown in Sec. B;
- Ablation studies on the proposed RND-HRNet and  $N$ -shot reconstruction (with  $N > 2$ ) are conducted in Sec. C;
- The limitations and broader impacts of this work are discussed and presented in Sec. D.

## Appendix A. Implementation Details of some Key Modules

### A.1. The pseudo codes of $\mathcal{H}_d(\cdot, \cdot)$ and $\mathcal{H}_d^\dagger(\cdot, \cdot)$ in the RNDM

To further reflect the forward and inverse operation of the imaging system, the PyTorch-style pseudo-codes of  $\mathcal{H}_d(\cdot, \cdot)$  and  $\mathcal{H}_d^\dagger(\cdot, \cdot)$  in the range-nullspace decomposition module (RNDM) are presented as follows.

```
def H_d(x, F): # shift and sum
    # input: x; shape: (B, C, H, W)  F; shape: (B, C, H, W)
    # output: y; shape: (B, 1, H, W+(C-1)*step)
    step = 2
    z = x * F
    y = zeros(B, 1, H, W)
    for i in range(C):
        y[:, :, :, i*step:i*step + W] += z[:, i:i+1]
    return y

def H_d_pinv(y, E): # rectification, cropping and sliding
    # input: y; shape: (B, 1, H, W+(C-1)*step)  E; shape: (B, C, H, W)
    # output: x; shape: (B, C, H, W)
    step = 2
    alpha = zeros(B, 1, 1, W+(C-1)*step)
    for i in range(C):
        alpha[:, :, :, i*step:i*step + W] += 1
    alpha = 1 / alpha
    z = y * alpha
    x = []
    for i in range(C):
        x.append(z[:, :, :, i*step:i*step + W])
    x = Concatenate(x, dim=1) / E
    return x
```

## A.2. Details of the CTB and STB in the SSFM

In this subsection, we elaborate on the details of the CTB and STB in Fig. 10 to show how the SSFM fuses spatial and spectral correlations adaptively. Following the previous work [6], the channel-wise transformer block (CTB) aims to extract spectral correlation, which includes two-layer normalization (LN) layers, one channel-wise self-attention (CSA) block and one feed-forward network (FFN). For convenience, we assume that the batch size is set to 1 respectively. Concretely, the CSA block encodes each feature frame  $\mathbf{I}_c$  to the channel-wise tokens via three linear layers to obtain the value  $\mathbf{V} \in \mathbb{R}^{HW \times C}$ , key  $\mathbf{K} \in \mathbb{R}^{HW \times C}$  and query  $\mathbf{Q} \in \mathbb{R}^{HW \times C}$  as follows.

$$\mathbf{Q} = \mathbf{I}_c \mathbf{W}_Q, \mathbf{K} = \mathbf{I}_c \mathbf{W}_K, \mathbf{V} = \mathbf{I}_c \mathbf{W}_V, \quad (20)$$

where  $\mathbf{W}_Q$ ,  $\mathbf{W}_K$  and  $\mathbf{W}_V \in \mathbb{R}^{C \times C}$  respectively denote the learnable parameters. Then,  $\mathbf{Q}$ ,  $\mathbf{K}$  and  $\mathbf{V}$  are respectively split into  $N$  heads along the channel dimension, namely  $\mathbf{Q} = [\mathbf{Q}_1, \dots, \mathbf{Q}_N]$ ,  $\mathbf{K} = [\mathbf{K}_1, \dots, \mathbf{K}_N]$  and  $\mathbf{V} = [\mathbf{V}_1, \dots, \mathbf{V}_N]$ . Note that the channel dimension of each head is  $C/N$ . Then, we calculate the self-attention map  $\mathbf{A}_j$  for each head  $j$  as follows.

$$\mathbf{A}_j = \mathbf{V}_j \cdot \text{Softmax}(\sigma_j \mathbf{K}_j^T \mathbf{Q}_j), \quad j \in \{1, 2, \dots, N\}, \quad (21)$$

where  $\sigma_j \in \mathbb{R}$  is the learnable parameter to represent the variation of spectral intensity. Finally, the above output is reshaped and fused via a convolution and added with the results of position encoding  $\mathcal{H}_{pos}(\cdot)$ .

$$\mathbf{O}_c = \text{CSA}(\mathbf{I}_c) = [\mathbf{A}_1, \dots, \mathbf{A}_N] \mathbf{W} + \mathcal{H}_{pos}(\mathbf{V}), \quad (22)$$

where  $\mathbf{W} \in \mathbb{R}^{C \times C}$  is the learnable weight of the convolution. The position encoding  $\mathcal{H}_{pos}(\cdot)$  is composed of several depth-wise convolutions and GELU activation. Meanwhile, inspired by the previous work [63], the spatial-wise transformer block (STB) aims to introduce local biases and spatial cues for the long-range transformer blocks via the sliding-window-based attention mechanism and residual blocks. Specifically, the input feature is firstly processed via an  $1 \times 1$  convolution and split in the channel dimension as follows.

$$\mathbf{I}_s^{(1)}, \mathbf{I}_s^{(2)} = \text{Split}(\text{Conv}(\mathbf{I}_s)). \quad (23)$$

One part of the split feature is fed to the Swin transformer block [26, 30] to explore the spatial correlation and non-local information. Additionally, the other part of the feature is fed to the residual block to capture local image cues. Finally, the two parts of features are fused adaptively via an  $1 \times 1$  convolution as follows.

$$\mathbf{O}_s^{(1)}, \mathbf{O}_s^{(2)} = \text{SwinT}(\mathbf{I}_s^{(1)}), \text{RB}(\mathbf{I}_s^{(2)}), \quad (24)$$

$$\mathbf{O}_s = \text{Conv}([\mathbf{O}_s^{(1)}, \mathbf{O}_s^{(2)}]) + \mathbf{I}_s, \quad (25)$$

where  $\text{SwinT}(\cdot)$  and  $\text{RB}(\cdot)$  respectively denote the operation of sliding-window-based transformer block and residual block.

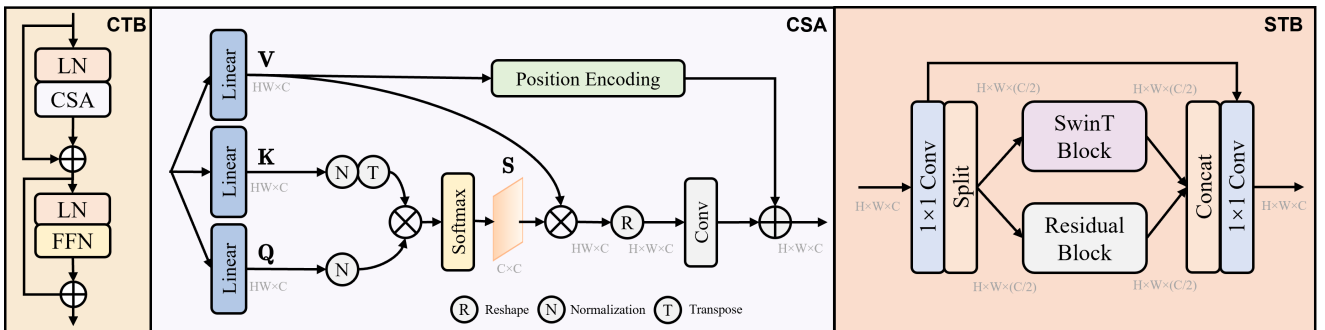


Figure 10. The details of channel-wise transformer block (CTB) and spatial-wise transformer block (STB) in the spectral-spatial fusion module (SSFM). These two blocks allow the SSFM to explore spectral and spatial correlation and fuse local and non-local information.

## Appendix B. Visualization Results

### B.1. Real Data and Simulation Results Visualization

To objectively evaluate the proposed RND-HRNet on real data, we present more visualization results with sufficient comparison methods [36, 34, 22, 20, 6, 5] and more band numbers in 2 real measurements [22]. To simulate the real imaging situations, 11-bit shot noise is injected into the training data [34]. As shown in Fig. 11, our results are more perception-friendly with clearer HSI contents and fewer artifacts. For instance, our results in the cropped regions of the flowers have smoother textures and our results in the cropped regions of the strawberries have less noise, which suggests the generalization ability and robustness of our method. Meanwhile, we also illustrate the other 3 real scenes [22] in Fig. 9 (right column). It can be clearly seen that our method can reconstruct high-quality hyperspectral images in different contents and degradations.

Furthermore, we present the two-shot simulation results of all the 28 bands [22] from 453.5nm to 648.0nm in Fig. 9 (right column). It proves that our results have accurate spectral information and smooth spatial details in different wavelengths.

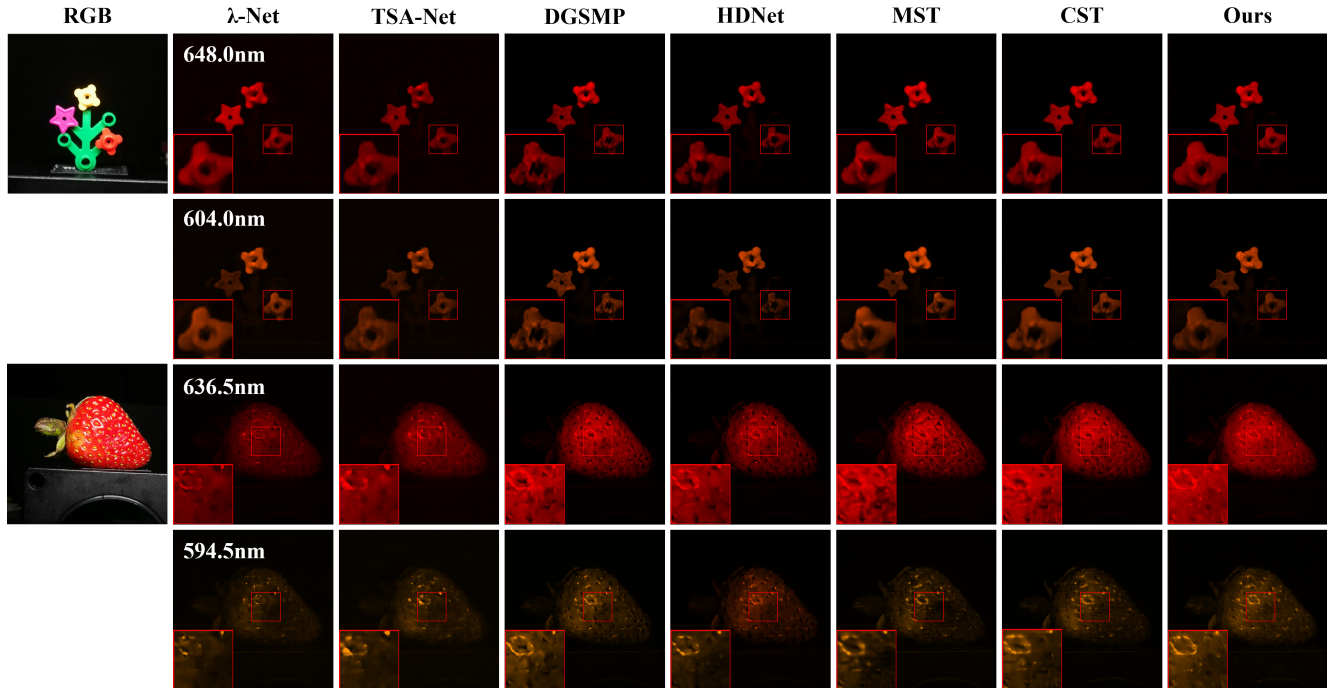


Figure 11. Real data results of the proposed RND-HRNet (Ours) and other SOTA methods on the single-shot reconstruction.

### B.2. Mask Visualization

To show the structure and data distribution of optimized coded apertures in different scenarios, we visualize more content-aware masks. As shown in Fig. 12, optimized masks  $M_1$  and  $M_2$  in three scenes are presented, where  $M_1$  is shared by all scenes and  $M_2$  is content-aware. Concretely,  $M_2$  is composed of the shared component  $\overline{M}_2$  and content-aware component  $\mathcal{H}'_M^{(2)}(y_1)$ . We find that although  $M_2$  remains a similar pattern, it veils some anisotropic HSI information of different scenes, which is conducive to the multiple-shot reconstruction.

Table 6. Evaluation of the effectiveness of different components.

Case Index	RNDM	CTB	STB	PSNR	SSIM
(a)	✗	✓	✓	35.13	0.951
(b)	✓	✗	✓	36.15	0.950
(c)	✓	✓	✗	36.10	0.953
(d)	✓	✓	✓	36.66	0.957

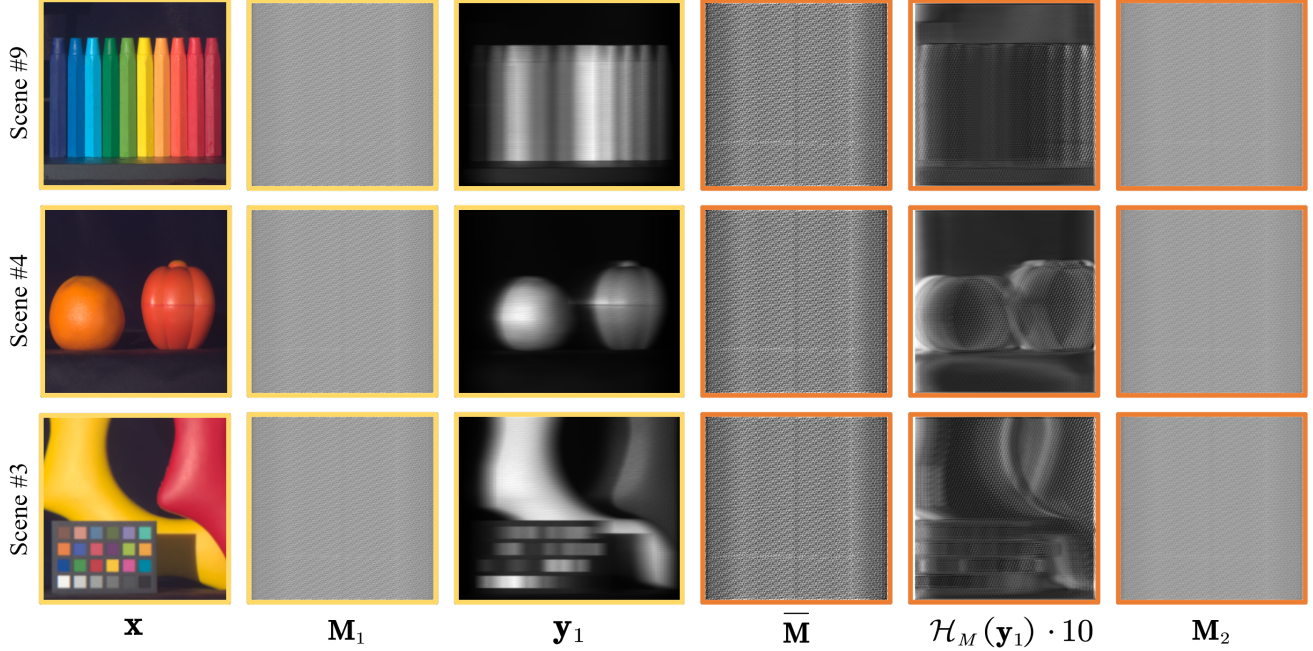


Figure 12. The visualization of the optimized content-aware masks  $\mathbf{M}_1 \in \mathbb{R}^{H \times W}$  and  $\mathbf{M}_2 \in \mathbb{R}^{H \times W}$ . The content-aware mask  $\mathbf{M}_2$  learns the anisotropic HSI information of different scenes adaptively with  $\mathbf{M}_2 = \bar{\mathbf{M}}_2 + \eta^{(2)} \cdot \mathcal{H}'_M^{(2)}(\mathbf{y}_1)$ , while the shared  $\mathbf{M}_1$  and  $\bar{\mathbf{M}}_2 \in \mathbb{R}^{H \times W}$  learn the general characteristics of the imaging system.

## Appendix C. More Ablation Studies

### C.1. Ablation Study on the Proposed RND-HRNet

To evaluate the contribution of different components in the proposed RND-HRNet, we conduct an ablation study on the single-shot reconstruction with the two-phase reconstruction network. We mainly focus on our adopted three modules, namely range-nullspace decomposition module (RNDM), channel-wise transformer block (CTB), and spatial-wise transformer block (STB). Tab. 6 illustrates the PSNR (dB) and SSIM on the different settings. Removing the RNDM, we retrained a variant of the proposed model that contains only two proximal mapping modules. It can be clearly seen that the PSNR has a decline of 1.43dB, proving the effectiveness of the proposed RNDM. Meanwhile, we respectively remove the CTB and STB in the SSFM to implement two variant models, namely case (b) and case (c). Obviously, without CTB, the values of the PSNR and SSIM have dropped by 0.51dB and 0.007 respectively. Without STB, the results of PSNR and SSIM have decreased by 0.56dB and 0.004. It further proves that integrating the spectral and spatial correlation cooperatively in the SSFM is necessary and significant for reconstruction quality.

### C.2. Ablation Study on the $N$ -shot Reconstruction

To explore the upper bound of the proposed progressive sampling in the multiple-shot reconstruction, we retrain the proposed PCA-CASSI when the shot number  $N$  is set to be 2, 3, 4, 5, and 6. The values of PSNR and SSIM are reported in Fig. 13. As the shot number increases, the reconstruction performances of the proposed PCA-CASSI are improved correspondingly and reach the peak when the shot number is set to 5. However, as the shot number increases above 5, the PSNR and SSIM results decline slightly due to the increased parameters and the network overfitting. Furthermore, it can be clearly seen from Fig. 14 that with the shot number increases, more HSI contents will be reflected in the coded apertures, which is conducive to the HSI reconstruction.

## Appendix D. Limitations and Broader Impacts

Limited by the quality of the hardware devices and the scarcity of real hyperspectral data, the core contribution of our paper focuses on designing a novel high-quality imaging framework and the proposed progressive sampling is mainly verified in the simulation setup, which will inspire future work in the community. However, we maintain that the proposed PCA-CASSI

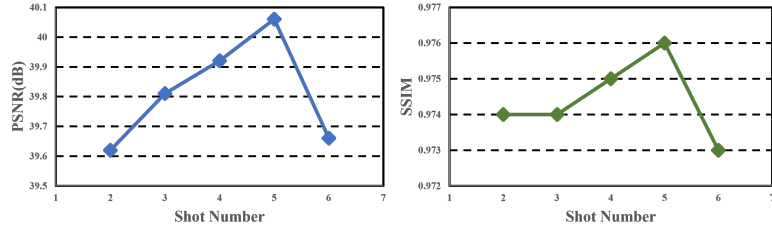


Figure 13. The values of PSNR and SSIM of the proposed PCA-CASSI on the  $N$ -shot reconstruction.

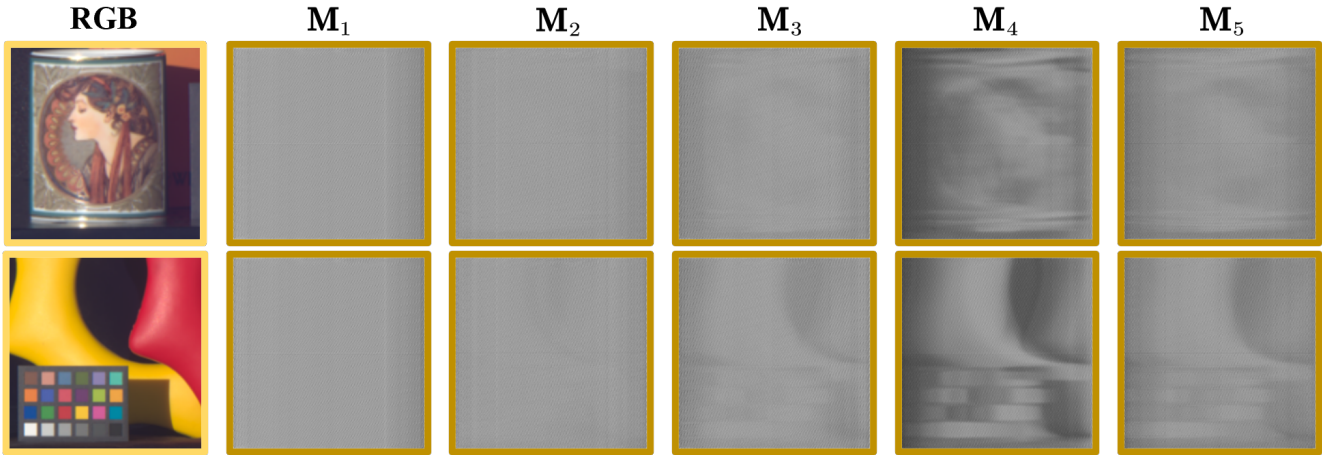


Figure 14. The visualization of five optimized content-aware masks on the 5-shot HSI reconstruction.

can be easily deployed on existing imaging systems such as [40]. We will realize the proposed PCA-CASSI in hardware imaging devices and present some real data results in our future work.

The proposed PCA-CASSI contributes to the industrial application of hyperspectral compressive imaging and inspires the design of deep unfolding networks in other image inverse problems such as video snapshot compressive imaging [50], super-resolution [32], and general image restoration [37]. Meanwhile, benefiting from its fast imaging speed and accurate HSI reconstruction, the proposed PCA-CASSI has the potential to promote closer integration of artificial intelligence in life sciences and cytology.